Modular Multilevel Converter and Parallel Hybrid Converter Based Open-End Windings AC Machine Drive for Wide Speed Range

Nageswara Rao Karaka, *Student Member, IEEE*, Ibhan Chand Rath, *Student Member, IEEE*,
and Anshuman Shukla, *Senior Member, IEEE*

***Abstract*—The parallel hybrid converter (PHC) is a potential alternative to the modular multilevel converter (MMC) for medium-voltage (MV) drive applications due to its remarkable features of lower static energy storage, fewer devices, and zero-voltage switching. Interestingly, for PHC-based variable speed drives, the submodule capacitor voltage ripple (CVR) is not highly affected by the operating speed, unlike MMC drives. However, in PHC drives, the current shoot-through in the dc-link is inevitable for variable motor voltage when the dc voltage source is stiff, which restricts the operating speed range of the drive. Hence, this article proposes a transformerless MMC–PHC drive configuration for open-end stator winding ac machines. The MMC acts as an active front-end converter that generates variable dc-link voltage to feed the motor-side converter while maintaining grid-side control targets. A coordinated control strategy between the PHC and MMC sides is proposed to achieve their control targets. The proposed drive configuration also offers regenerative operation. A comparative static energy storage analysis between the proposed and existing state-of-the-art MV drives is presented to verify its effectiveness. The proposed configuration and control strategy are evaluated for different operating conditions, including dynamic load change and regenerative operation, using both simulation and experimental studies.**

***Index Terms*—Back-to-back (BTB) drive configuration, high power drives, medium-voltage (MV) drives, modular multilevel converter (MMC), parallel hybrid converter (PHC).**

I. Introduction

MEDIUM-VOLTAGE (MV) multilevel voltage source converters are the potential candidates to meet the increasing power demand of multimega-watt industrial drives such as compressors and pumps in the oil and gas industry, bucket wheel excavators in mines, etc. [1], [2], [3], [4], [5], [6]. Industrial variable speed drives (VSDs) are gaining importance due to energy conservation and economic savings [6], [7], [8]. In recent years, modular multilevel converter (MMC) based VSDs have become popular due to their low harmonic distortion, high efficiency, modularity, and reliability [6], [8], [9], [10], [11], [12]. The MMC based drives can operate with a single direct voltage bus instead of isolated dc sources as required in the conventional cascaded H-bridge-based drives [4], [6]. Benshaw [13] and Siemens [14] have successfully commercialized MMC-based drives across various power levels and voltages. However, the MMC drive has a high submodule capacitor voltage ripple (SMCVR) during low-speed operation [9], [10], [15], [16], [17]. Also, it requires high static energy storage.

Various techniques have been presented in the literature to ensure the SMCVR is within the limits for low-speed operation of MMC-based drives [9], [10], [16], [17], [18], [19], [20], [21], [22]. The predominant solutions are the common mode voltage (CMV) and circulating current (CC) injection technique as in [9], [16], [18], [22], and [23]. This technique effectively reduces the capacitor voltage ripple (CVR) at all speeds, but at the cost of huge device current stress and bearing currents due to the CMV as noted in [6] and [18]. To minimize these issues, He et al. [17] present an improved injection of CMV and CC using full-bridge SM (FBSM) MMC drive. This approach still has significant current stress. Further, Sau and Fernandes [10] demonstrate the multipulse diode-bridge rectifier-fed MMC drive with stepped variation of dc-link voltage of the MMC drive. However, a momentary zero power transfer control for the stepped transition of the dc-link voltage leads to control complexities. Additionally, Li et al. [43] introduce a variable average dc-link voltage technique using a dc-chopper switch-based hybrid-MMC drive. This method features a low SMCVR and reduces the need for CVR suppression techniques. However, this method suffers from discontinuous dc-link current, necessitating additional dc-filters and overvoltage protection circuits.

In [20], the CMV injection-free back-to-back (BTB) FBSM MMC–MMC-based drive control strategy is presented. The front-end MMC maintains rated dc-link current throughout the speed range and varies the dc-link voltage. The SMCVR is kept constant for full speed range, including regenerative operation. However, this technique requires a rated dc-link current even during the low load torque. Also, it involves FBSM-based MMC on both sides, leading to higher devices and higher capacitive energy storage. Further, Li et al. [44] present a BTB hybrid-MMC drive using FBSMs in upper arm of grid side MMC, and

---

Received 17 December 2024; revised 7 April 2025 and 30 June 2025; accepted 7 August 2025. Date of publication 25 August 2025; date of current version 13 November 2025. This work was supported by the TRC Deeptech IIT Bombay Project under Grant 'RD/0524-IOETR00-003'. Recommended for publication by Associate Editor D. G. Xu. *(Corresponding author: Anshuman Shukla.)*

Nageswara Rao Karaka and Anshuman Shukla are with the Department of Electrical Engineering, IIT Bombay, Mumbai 400076, India (e-mail: k_nageswar@iitb.ac.in; ashukla@ee.iitb.ac.in).

Ibhan Chand Rath is with Igrenenergi Services Private Limited, Research Park, IIT Bombay, Mumbai 400076, India (e-mail: ibhanchand.rath@igrenenergi.com).

Color versions of one or more figures in this article are available at https://doi.org/10.1109/TPEL.2025.3602463.

Digital Object Identifier 10.1109/TPEL.2025.3602463

half-bridge SMs (HBSMs) in lower arms of grid side as well as in upper and lower arms of motor-side MMC, hence saves the number of devices compared to that in [20]. However, the control is complicated due to the asymmetry of the grid-side converter (GSC). In [11], a BTB hybrid-MMC drive is presented using hybrid SMs (combination of HBSMs and FBSMs) on grid-side and HBSM-based MMC on motor-side to ensure symmetry as well as to minimize the SMCVR. However, this approach still requires higher capacitive energy storage than the conventional MV drives. In [21], cascaded MMC and cyclo-converter (CCV) based drive configuration is presented to avoid the need for the injection technique. The MMC generates medium-frequency ac voltage as an input to the CCV. The CCV converts this medium-frequency input to the low-frequency ac voltage to feed the motor. It requires low capacitive energy storage but introduces harmonic components in motor currents due to the phase-controlled thyristor operation. This leads to excessive torque ripple, which is undesirable in MV drives.

To minimize the capacitive energy storage and avoid CC issues, a parallel hybrid converter (PHC) drive is a potential alternative to the MMC-based drives [24], [25], [26]. The PHC drive offers several advantages including fewer power devices, zero-voltage switching (ZVS), and high power-to-weight ratio [24]. However, for variable ac voltage, current shoot-through in the dc-link is inevitable when the dc voltage source is stiff [24], [25], [26], restricting the variable speed capabilities of PHC–MV drives. Recently, for a PHC-based VSD presented in [26], a third-harmonic voltage injection based technique is implemented to vary ac voltage. However, this necessitates the need for an isolation transformer even for open-end stator winding ac machines (OEWMs), oversizing the chain-link (CL) by 1.5 times in voltage rating and 1.33 times in current rating [25], making it less practical for MV drives.

To address some of the major aforementioned issues faced by the MV drives, this article proposes a transformerless MMC–PHC drive configuration for the OEWMs to achieve wide-speed operation without oversizing the PHC while keeping its inherent merits. The main contributions of the presented article are as follows.

1) A new transformerless MMC–PHC drive configuration is proposed for a wide speed range of operation without need of huge injection of CC current and CMV.
2) A new control technique is proposed for synthesizing a wide range of variable dc-link voltage using the FBSM-based MMC.
3) A control strategy is proposed for coordinating control targets of the grid side and motor side such as overall PHC energy balancing control, individual CL energy balancing control, dc-link current control, field-oriented control of the motor, and voltage-oriented control of the grid.
4) The proposed drive configuration and control strategy are validated for various operating points, including dynamic load change and regenerative operation, using the simulation and experimental studies.
5) A comparative static energy storage analysis between the proposed and existing state-of-the-art modular MV drives is presented to verify its effectiveness.

The rest of this article is organized as follows. The operation of the proposed drive configuration and the various design aspects of its SMs capacitor are presented in Section II. The proposed control strategy for coordinating control targets is described in Section III. A simulation study is carried out in PSCAD to validate the proposed drive configuration along with its claimed features and control strategy, and the results are discussed in Section IV. The proposed work is further validated using a scaled-down experimental prototype developed in the laboratory, and the corresponding experimental study results are presented in Section V. Finally, Section VI concludes this article.

II. OPERATION AND DESIGN OF THE PROPOSED MMC–PHC DRIVE CONFIGURATION

The proposed three-phase MMC–PHC drive configuration is illustrated in Fig. 1. The MMC GSC rectifies the grid-connected ac voltage (v_g^x) into a variable dc-link voltage (v_{dc}) to form a common direct voltage bus (z-z'). It comprises six arms, each with a series connection of FBSMs. They generate an appropriate arm voltage (v_u^x) to synthesize v_{dc} from the converter ac-side voltage (v_{gsc}^x). Further, the PHC drive [motor-side converter (MSC)] inverts the dc-link voltage (v_{dc}) into an ac voltage (v_x) with the desired frequency (f) to feed the ac machine. The PHC drive has three CLs connected in series to support the common dc-link. Each CL consists of a cascade of HBSMs to generate the CL voltage (v_{CL}^x), which is a rectified waveform of the motor voltage (v_x). The v_{CL}^x gets unfolded by using an H-bridge to synthesize the sinusoidal motor voltage (v_x). The switches ($S_{x1}$to S_{x4}) in the H-bridge have to withstand the amplitude of the motor voltage ($\hat{V}_m$). For MV drives up to 13.6 kV, two or three 6.5 kV IGBTs can be connected in series to realize S_{x1} which is industry practice. Even for higher voltage drives, the realization of S_{x1} can be easily achievable by the matured engineering solutions [27], [35], [36], [37], [38], [39], [40]. Further, these switches operate at the motor's fundamental frequency (f) and operate at zero crossing of the motor voltage (v_x) to achieve the ZVS operation. The three-phases of OEWM are connected across the ac terminals (X-X', $X = A, B$, and C phases) of the unfolding H-bridge. Consequently, the OEWM provides isolation among the ac terminals of the unfolding H-bridge owing to the series connection of CLs. To apply the proposed work to Y-connected standard machines, they can be modified to open-end stator windings at the terminal box.

A. Operation of the PHC Drive (Motor-Side Converter)

In the proposed drive configuration, Fig. 1, one CL for each phase is formed by a series connecting N_p number of HBSMs. Each CL generates a rectified voltage (v_{CL}^x) with 120^0 phase-shift with respect to each other. Also, these three CLs are connected in series across the dc-link terminals (z-z') via an inductor (L_{dc}). The role of L_{dc} is to ensure that the instantaneous voltage of v_{TCL} closely matches the v_{dc} [24]. The v_{CL}^x and the instantaneous total CL voltage (v_{TCL}) can be expressed as

$$v_{\text{CL}}^x = n_{\text{CL}}^x\, v_{c,x}^{\Sigma} = \hat{V}_m\, \left|\sin\left(\omega t - \theta_x\right)\right| \tag{1a}$$

$$n^{px} = k\left|\sin\left(\omega t - \theta_x\right)\right| \tag{1b}$$

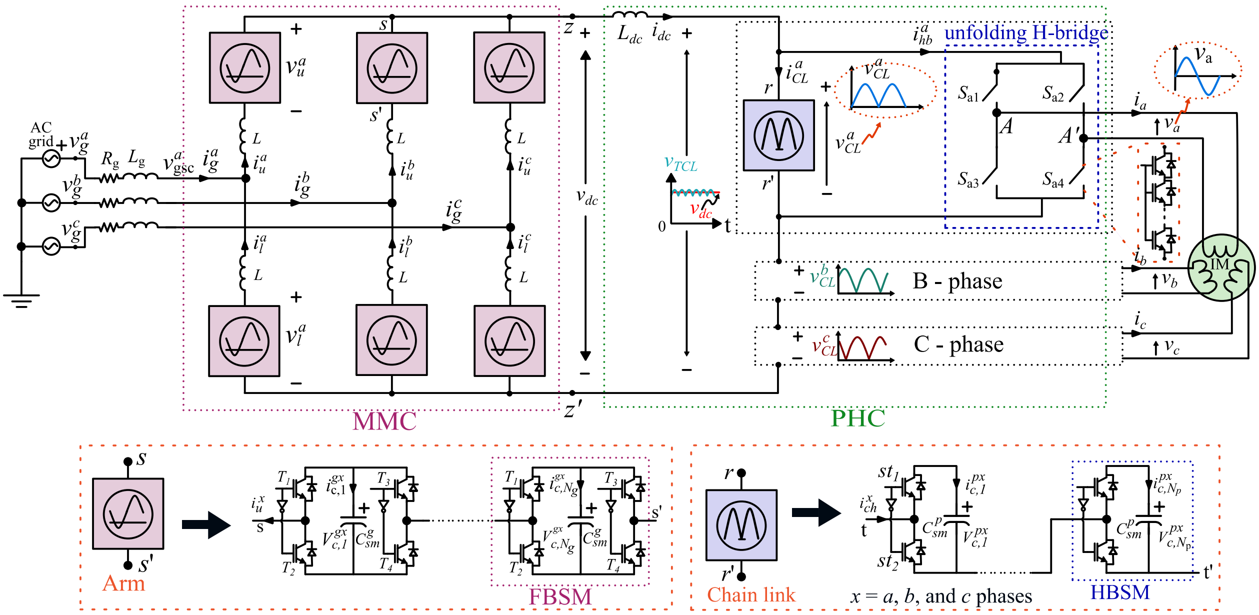

Fig. 1. Proposed MMC–PHC drive configuration for AC motors.

$$v_{\text{TCL}} = \sum_{x=a,b,c} v_{\text{CL}}^x \tag{2}$$

where $v_{c,x}^{\Sigma}$ is the sum of voltages of all SM capacitors in a CL, n_{CL}^x is the insertion index of the CL, $\hat{V}_m(=kv_{c,x}^{\Sigma})$ is the amplitude of the motor voltage, k is the voltage fraction of the rated $\hat{V}_m$, ω is the fundamental angular synchronous frequency of the motor, and phase-shift θ_x assumes the value of $0^\circ, 120^\circ,$ and 240° of $x = a, b, c$ phases, respectively. For the SPWM modulation, the voltage $\hat{V}_m$ is expressed as in (3) in terms of modulation index (m) and the dc-link voltage (V_{dc}). From (1) to (3), the average value of the total CL voltage (V_{TCL}) over a fundamental cycle is obtained as in (4). By applying Kirchhoff's voltage law in the dc-link loop (Fig. 1), the i_{dc} dynamic equation can be written as in (5):

$$\hat{V}_m = \frac{mV_{\text{dc}}}{2} \tag{3}$$

$$V_{\text{TCL}} = \frac{6}{\pi}\,\hat{V}_m = \frac{3}{\pi}\,mV_{\text{dc}} \tag{4}$$

$$\frac{di_{\text{dc}}}{dt} = \frac{1}{L_{\text{dc}}}\,(v_{\text{dc}} - v_{\text{TCL}})\,. \tag{5}$$

From (5), the average value of the dc-link voltage (V_{dc}) and the total CL voltage (V_{TCL}) must be equal irrespective of the operating point for stable operation of the system. This implies that, from (4), the m value should be equal to $\pi/3$ for all operating points. Hence, the V_{TCL} or motor voltage (v_x) cannot be varied otherwise, a shoot-through in the dc-link current (i_{dc}) would be the result. To overcome this, a third-harmonic voltage injection technique has been presented in the literature [25] and [26]. However, this technique requires oversizing the PHC drive to achieve the full range of variable v_x as stated in Section I.

In this article, the variable v_x is obtained by varying v_{dc} based on the proposed overall PHC energy balancing controller and an i_{dc} controller. The variable v_{dc} is synthesized using the FBSMs-based MMC as the GSC without compromising control over the grid-side control targets such as P_g and unity power factor. The proposed method features an injection-free regenerative modular drive system with low energy storage requirements. Also, the GSC features the dc-link and motor fault tolerant operation due to the negative arm voltage capability [28]. The synthesis of the variable v_{dc} is analyzed in the next subsection.

B. Synthesizing Variable DC-Link Voltage

In the proposed drive configuration (Fig. 1), the three-phase grid-connected MMC synthesizes the desired v_{dc} across the dc-link terminals (z-z'). Each arm consists of N_g number of FBSMs for $N_g + 1$ levels of ac-side phase voltage. In an FBSM (Fig. 1), when T_1, T_4 are ON the capacitor voltage is positively inserted ($V_{\text{SM}} = +V_c$), when T_1, T_3 or T_2, T_4 are ON the capacitor is bypassed ($V_{\text{SM}} = 0$), and when T_2, T_3 are ON the capacitor is negatively inserted ($V_{\text{SM}} = -V_c$). The dynamics of the grid-connected GSC can be expressed as [28]

$$v_{ul}^x = \mp v_{\text{gsc}}^x + 0.5V_{\text{dc}} + L\frac{di_{ul}^x}{dt} \tag{6a}$$

$$v_{\text{gsc}}^x = 0.5 \times (v_l^x - v_u^x) \tag{6b}$$

$$v_{\text{gsc}}^x = V_g^x - R_g i_g^x - L_g\frac{di_g^x}{dt} \tag{6c}$$

$$v_g^x = \hat{V}_g \sin\left(\omega_g t - \theta_g^x\right) \tag{6d}$$

$$V_{\text{dc}} = v_u^x + v_l^x = n_u^x v_{c,u}^{x\Sigma} + n_l^x v_{c,l}^{x\Sigma} \tag{6e}$$

$$\hat{V}_{\text{gsc}} = \frac{m_{\text{gsc}} v_{\text{dc}}}{2} \tag{6f}$$

where v_{gsc}^x is the phase voltage at ac-terminals (abc) of the GSC, V_{dc} is the dc-link voltage, m_{gsc} is the modulation index of the GSC, i_{ul}^x is the upper (u) and lower (l) arm currents, v_g^x is

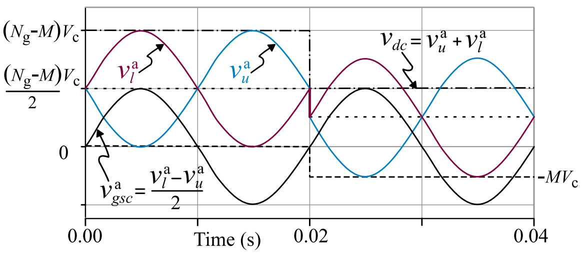

Fig. 2. Proposed operating waveforms of the grid-side converter (GSC).

the grid phase voltage, i_g^x is the grid currents, θ_g^x is 0°, 120°, and 240° of $x = a, b,$ and c phases, respectively, ω_g is the grid angular frequency, and L and L_{g} are the arm and grid inductances, respectively. When the motor voltage (v_x) or speed (ω_r) decreases, the voltage v_{dc} has to be decreased as discussed in Section I-A. In typical GSCs such as NPC, active-NPC, and HBSM-based MMC, the output voltage (v_{dc}) will always be greater than the peak value of the line–line grid voltage ($\sqrt{3}\hat{V}_{\text{gsc}}$). When the desired v_{dc} is less than the $\sqrt{3}\hat{V}_{\text{gsc}}$, the anti-parallel diodes across IGBTs will get forward bias all the time, and the v_{dc} will be $\sqrt{3}\hat{V}_{\text{gsc}}$, and no control over the output voltage [29]. Nevertheless, in the case of the FBSM-based MMC rectifier, a wide range of variable v_{dc} can be achieved by the negative insertion capability of SM. The constraint $v_{\text{dc}} > \sqrt{3}\hat{V}_{\text{gsc}}$ is ensured for a wide range of variable v_{dc}operation by reducing the effective ac voltage involved in the rectification process thanks to the negative arm voltage (v_{ul}^x) capability. In other words, from (6b), the dc-link voltage (v_{dc}) can be varied by adjusting the dc-offset of the arm voltage ($0.5V_c(N_g - M)$) as in Fig. 2, even if the converter voltage v_{gsc}^x is of rated value. When v_{dc} decreases with rated v_{gsc}^x, from (6f), the modulation index (m_{gsc}) can be linearly extended beyond unity up to ($2N_m - 1$) as in (7) using negative insertion of SMs (M). The modulation index and the average voltage of the SM capacitor (V_c) will then be

$$m_{\text{gsc}} = \frac{N_g + M}{N_g - M} \tag{7}$$

$$V_c = \frac{v_{\text{dc}}}{N_g - M} = \frac{V_{\text{dc}}^{\text{rated}}}{N_g} \tag{8}$$

where M is the number of negatively inserted SMs (a subset of N_g) for voltage v_{dc}. From (8), the V_c can be maintained constant by using M number of SMs while varying the v_{dc}. The static energy requirement of the proposed configuration is presented in the following subsection for the variable v_{dc} and the motor speed (ω) based on the SMCVR.

C. Voltage Ripple of SMs Capacitor of MSC

The SMCVR is vital in selecting the capacitance value. Due to the symmetry among the three CLs, only the a-phase of the PHC drive is considered here for analysis. From Fig. 1, the SMs capacitor current ($i_{c,1}^{pa}$) and voltage ($v_{c,1}^{pa}$) in the CL can be expressed as in (10)

$$i_{c,1}^{pa} = n^{pa} \times i_{\text{CL}}^{a} \tag{9a}$$

$$i_{\text{CL}}^{a} = \begin{cases} i_{\text{dc}} - \hat{I}_m \sin(\omega t - \phi), & 0 \le t < 0.5T \\ i_{\text{dc}} + \hat{I}_m \sin(\omega t - \phi), & 0.5T \le t < T \end{cases} \tag{9b}$$

$$v_{c,1}^{pa} = \frac{1}{C_{sm}^{p}} \int i_{c,1}^{pa}.\text{dt} \tag{9c}$$

$$i_{\text{dc}} = \frac{\pi}{4}\hat{I}_m \cos(\phi) \tag{9d}$$

where n_{CL}^a is the insertion index as expressed in (1b), i_{CL}^a is the a-phase CL current, i_{dc} is the dc-link current, $\hat{I}_m$ is the peak value of the stator current, ϕ is the motor power factor angle, and C_{sm}^p is the capacitance value of the SM. The CVR ($\Delta V_{c,1}^{pa}$) is expressed as in (10). The extreme points (θ_1 and θ_2) of $\Delta V_{c,1}^{pa}$ occur at zero crossing instants of the SMs capacitor current, which also represents the same instants of zero crossing instants of the CL current (i_{CL}^a)

$$\Delta V_{c,1}^{pa} = \frac{1}{C_{\text{sm}}^{p}} \int_{\theta_1/\omega}^{\theta_2/\omega} i_{c,1}^{pa}.dt \tag{10a}$$

$$\theta_1 = |\phi| + \sin^{-1}\left(\frac{\pi\cos\phi}{4}\right) \tag{10b}$$

$$\theta_2 = |\phi| + \pi - \sin^{-1}\left(\frac{\pi\cos\phi}{4}\right). \tag{10c}$$

By solving (10), the final CVR $\Delta V_{c,1}^{pa}$ is obtained as in (11a), which is a function of stator current (I_m), power factor, and the k/ω ratio. Thus, the voltage ripple $\Delta V_{c,1}^{pa}$ will not be affected by the operating speed (ω) for VSDs due to the constant flux (k/ω = constant) operation

$$\Delta V_{c,1}^{pa} = \frac{I_m\cos\phi}{2C_{\text{sm}}^{p}}\left(\frac{k}{\omega}\right)\left[\frac{\pi\cos\phi}{2}\sqrt{1-\left(\frac{\pi\cos\phi}{4}\right)^2} - \pi + 2\sin^{-1}\left(\frac{\pi\cos\phi}{4}\right)\right] \tag{11a}$$

$$E_{\text{nom}}^{p} = 0.5C_{\text{sm}}^{p}(V_c^{pa})^2 N_p \times 3. \tag{11b}$$

To account for the worst scenario, constant rated load torque and all possible operating power factors are considered. For a typical allowable CVR of 0.1 p.u., the SM capacitance C_{sm}^p is calculated for the entire speed range. The C_{sm}^p value is substituted in (11b) to calculate the energy storage per unit power, illustrated in Fig. 3. Notably, it is evident that the energy storage requirement in the PHC drive is approximately eight times (4.5 kJ/MVA) smaller than that in the MMC drive (38.32 kJ/MVA) for satisfying the full speed range.

D. Voltage Ripple of SMs Capacitor in GSC

For the a-phase upper arm of GSC (Fig. 1), the SM capacitor current and voltage are given as follows:

$$i_{c,1}^{ga} = n_u^a \times i_u^a \tag{12a}$$

$$n_u^a = \frac{v_u^a}{v_{c,u}^{a\Sigma}} = [-m_{\text{gsc}}\sin(\omega_g t - \delta) + k] \times 0.5 \tag{12b}$$

$$i_u^a = \frac{i_{\text{dc}}}{3} + 0.5\hat{I}_g \sin(\omega_g t - \phi_g) \tag{12c}$$

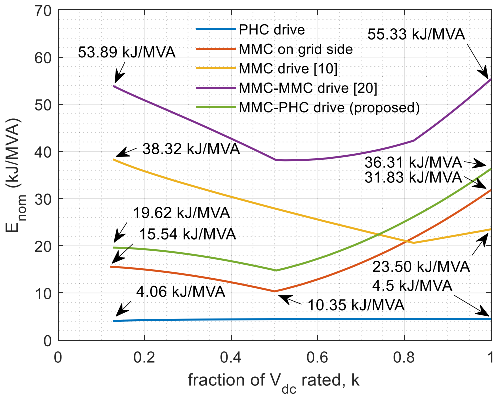

Fig. 3. Comparison of capacitive energy storage of proposed MMC–PHC drive over MMC–MMC drive.

$$\frac{i_{\mathrm{dc}}}{3} = \frac{m_{\mathrm{gsc}}}{4}\,\hat{I}_g\cos(\phi-\delta) \tag{12d}$$

$$v_{c,1}^{ga} = \frac{1}{C_{\mathrm{sm}}^{g}}\int i_{c,1}^{ga}.\mathrm{dt} \tag{12e}$$

where δ is the phase angle between the grid voltage v_g^x and converter voltage v_{gsc}^x, k is the fraction of the rated dc-link voltage, n_u^a is the arm insertion index of an SM, and $\hat{I}_g$ is the amplitude of the grid current. Using (12), the capacitor voltage $v_{c,1}^{ga}$ can be written as follows:

$$\begin{aligned} v_{c,1}^{ga} &= \frac{k\hat{I}_g}{4C_{\mathrm{sm}}^{g}\omega_g}\Bigg[-\cos(\omega_g t-\phi_g)+\frac{m_{\mathrm{gsc}}^2}{2}\cos(\phi_g-\delta) \\ &\quad\times\cos(\omega_g t-\delta)+\frac{m_{\mathrm{gsc}}}{4}\sin(2\omega_g t-\delta-\phi_g)\Bigg]+V_c^{ga} \end{aligned} \tag{13a}$$

$$E_{\mathrm{nom}}^{g} = 0.5C_{\mathrm{sm}}^{g}(V_c^{ga})^2 N_g\times 6. \tag{13b}$$

From (13a), the capacitor voltage is the function of k, $\hat{I}_g$, δ, and ϕ_g. The extreme points of the capacitor voltage $v_{c,1}^{ga}$ occur at zero crossing instants of capacitor current $i_{c,1}^{ga}$. This could happen at zero crossing instants of both arms' current i_u^a and insertion index n_u^a. Due to the derivation complexity, the graphical approach is chosen. The $\hat{I}_g$ varies with active power, and all possible power factors are considered to account for the worst scenarios. For the typical value of the voltage ripple ($\Delta v_{c,1}^{ga}$) of 0.1 p.u., the minimum capacitance value (C_{sm}^{g}) is calculated and substituted in (13b) to calculate the static energy storage per unit of power for various values of k as shown in Fig. 3. It can be inferred from Fig. 3 that the GSC (MMC on the grid side) has the requirement of 31.8 kJ/MVA of static energy.

Additionally, for comparative analysis, the energy storage requirement of both the proposed MMC–PHC configuration (comprising GSC and MSC stages) and MMC–MMC configuration [20] are depicted in Fig. 3. It is evident that the total energy storage required for the proposed MMC–PHC configuration is 36.31 kJ/MVA, which is significantly lower than that for the existing MMC–MMC drive (55.33 kJ/MVA). This analysis further highlights that the proposed configuration is a promising solution as it demands lesser energy storage.

E. Design of the DC-Link Inductance Value

From (2), the v_{TCL} is a six-pulse rectified voltage that has $6n$ harmonic components and can be expressed as

$$v_{\mathrm{TCL}} = 2\hat{V}_m\cos(\omega t-\pi/6)\,,\; 0\le t\le \pi/(6\omega)\,. \tag{14}$$

These harmonic voltage components generate their current components in the dc-link current ripple as in (5). The dc-link inductor, L_{dc} is used to minimize this ripple current. Form (5), the peak-to-peak dc-link current ripple is expressed as

$$\begin{aligned} \Delta I_{\mathrm{dc}} &= \frac{1}{L_{\mathrm{dc}}}\int_{t_1}^{t_2}(v_{\mathrm{dc}}-v_{\mathrm{TCL}})\,.dt \\ t_1 &= \frac{\frac{\pi}{6}-\cos^{-1}\left(\frac{3}{\pi}\right)}{\omega} = \frac{0.2222}{\omega}, \\ t_2 &= \frac{\frac{\pi}{6}+\cos^{-1}\left(\frac{3}{\pi}\right)}{\omega} = \frac{0.82497}{\omega} \end{aligned} \tag{15}$$

where t_1 and t_2 are the extreme instants of the dc-link current ripple which are the same as the zero crossing instants of $(v_{\mathrm{dc}}-v_{\mathrm{TCL}})$. By substituting (4) and (14) in (15), the peak-to-peak dc-link current ripple is expressed as

$$\Delta\, I_{\mathrm{dc}} = \frac{0.0362\hat{V}_m}{\omega L_{\mathrm{dc}}}. \tag{16}$$

To limit the peak-to-peak dc-link current ripple within the permissible value (typically 10%), the dc-link inductance value can be expressed as

$$L_{\mathrm{dc}} = \frac{0.0362\hat{V}_m}{\omega\times\left(0.1\times I_{\mathrm{dc}}^{\mathrm{rated}}\right)}. \tag{17}$$

Note that, from (16), the dc-link current ripple will not be affected by the motor operating frequency due to the constant $\hat{V}_m/\omega$ ratio in drive applications. The control strategy for both sides of the converters is described in the following section.

III. PROPOSED CONTROL STRATEGY FOR MMC–PHC DRIVE

On the MSC, the control targets are the vector control of rotor speed and flux component of currents, overall energy balancing of the CLs, and balancing the SMCVs within and among the CLs. Further, the GSC must achieve control targets such as active and reactive power components of currents and balance the SMCVs within the phases. The analysis of these controls is described as follows.

A. Control of Rotor Speed and Flux

The speed (ω_r) and flux component of current (i_{sd}^*) controllers are implemented using the rotor flux-oriented control of the induction motor [30], as shown in Fig. 4. The speed controller produces the torque component of the current i_{sq}^*. The i_{sq}^* and i_{sd}^* currents are controlled using PI controllers to produce reference voltages. Further, the cross-coupling terms (18) are

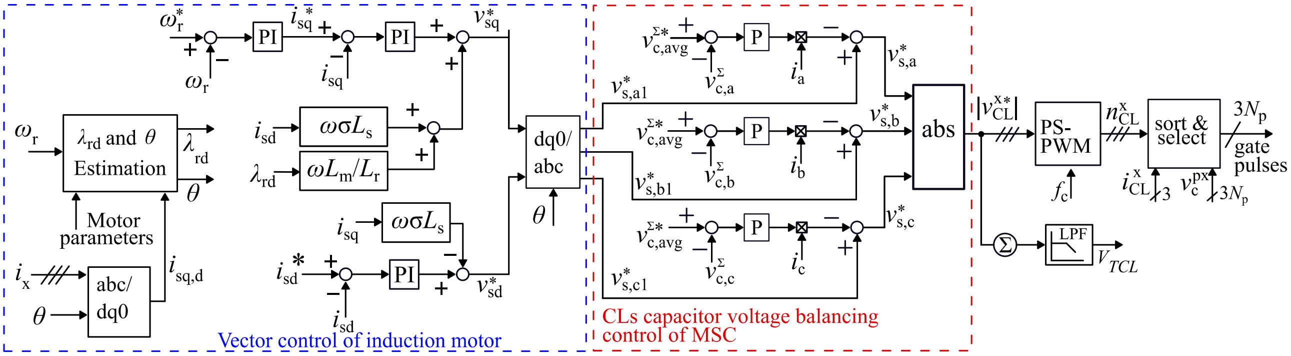

Fig. 4. Control of proposed motor side converter.

decoupled from the reference voltages to obtain the actual stator voltage components v^*_{sq} and v^*_{sd}. They are transformed into *abc* components $v^*_{s,x1}$ using the estimated rotor flux position (θ). The rotor flux and its position (θ) are computed using indirect flux estimation [30]

$$v'_{sq} = \omega \frac{L_m}{L_r}\lambda_{rd} + \omega\sigma L_s i_{sd} \tag{18a}$$

$$v'_{sd} = \frac{L_m}{L_r}\frac{\mathrm{d}}{\mathrm{dt}}\lambda_{rd} - \omega\sigma L_s i_{sq} \tag{18b}$$

where $\sigma = 1 - \frac{L_m^2}{L_r}$, $\lambda_{rd} = \frac{L_m}{1+s\tau_r} i_{sd}$.

B. CLs Capacitor Voltage Balancing Control

The SMCVs between the three CLs will not be equal in real-time systems due to the aging of the capacitors, dynamic load changes, device parameters mismatch, control and modulation errors, etc. This leads to unbalanced output voltage and unequal active power sharing among the phases. The control diagram for equalizing the SMCVs between the CLs is shown in Fig. 4 [32]. The sum of SMCVs of a CL is compared with its reference value and the error is passed through a proportional controller. The result is multiplied by the phase current i_x to account for the effect of the power factor. The final reference voltage $v^*_{s,x}$ is computed by adding the reference stator voltage $v^*_{s,x1}$ obtained from the motor controller.

Using $v^*_{s,x}$ and (2), the CL voltage v^x_{CL} is computed as illustrated in Fig. 4. The phase-shift pulsewidth modulation (PSPWM) [28] is used to obtain the CLs insertion index n^x_{CL}. Finally, the gate pulses for SMs are generated based on the conventional sorting and selection algorithm [28] depending on CLs current and SMCVs as illustrated in Fig. 4. This algorithm ensures uniform distribution of charge among the SM capacitors within a CL for all values of k.

C. Overall Energy Balancing Control of CLs of MSC

From Fig. 1, the power flow between the dc and ac sides of the MSC is controlled by maintaining sufficient stored energy in the total CLs of the MSC, as expressed in (19a). This can be further simplified as follows and its equivalent circuit is illustrated in Fig. 5

$$\frac{d}{dt}\left(\frac{1}{2}C^p_{\mathrm{eq}} v^2_{\mathrm{TCL}}\right) = p_{\mathrm{dc}} - p^{\mathrm{MSC}}_{\mathrm{ac}} \tag{19a}$$

$$C^p_{\mathrm{eq}}\frac{d}{dt}\left(v_{\mathrm{TCL}}\right) = i_{\mathrm{dc}} - i_L \tag{19b}$$

$$C^p_{\mathrm{eq}} = \frac{C^p_{\mathrm{sm}}}{(6N_p/\pi)} \tag{19c}$$

where C^p_{eq} is the equivalent capacitance across the total CL and i_L is the equivalent current responsible for the output power. From (19b), the available stored energy can be ensured by controlling v_{TCL}.

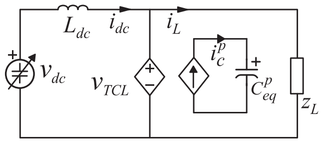

Fig. 5. Proposed coordinated control strategy for the MMC–PHC drive.

Using (19), the control diagram is presented in Fig. 5. The reference voltage (v^{p*}_c) would be the nominal value of the SMCV. The output of the v_{TCL} controller would be the dc-link current reference (i^*_{dc}). The control parameters are obtained by following the method given in [31].

D. DC-Link Current Control

As mentioned in Section II, the current i_{dc} should be controlled to avoid the shoot-through current in the inductor L_{dc}. The dynamic expression for this control is given in (5). From (5), the i_{dc} control diagram is illustrated in Fig. 6. The reference current i^*_{dc} is obtained from the overall energy balancing controller. The output of this controller is the reference voltage v^*_{dc} to be maintained by the GSC control, as shown in Fig. 6.

E. Control of Grid Side Converter (GSC)

The GSC control consists of active (p_g) and reactive power (Q_g) controllers. These have been implemented using the grid voltage-oriented vector control [28]. The active power is drawn from the grid or reference power p^*_g depends on the load on the

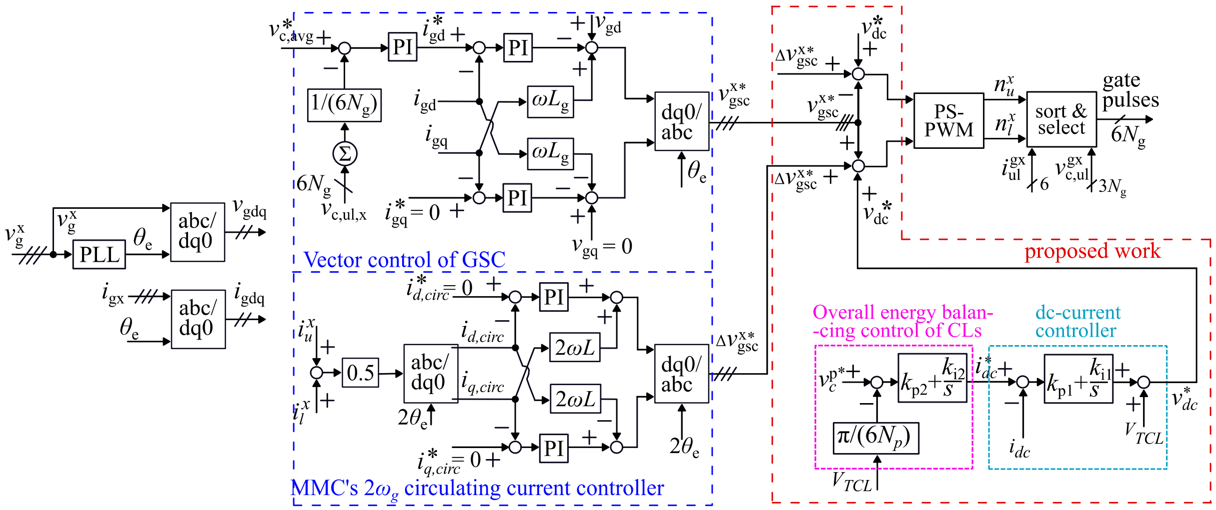

Fig. 6. DC equivalent circuit of the MSC.

motor. The active power p_g transfer between the ac and dc sides can be controlled by maintaining sufficient energy in the MMC's SM capacitors expressed as follows:

$$\frac{d}{dt}\left(\frac{1}{2}C_{\text{eq}}^{g}v_{\text{dc}}^{2}\right)=p_g-p_{\text{dc}} \tag{20a}$$

$$C_{\text{eq}}^{g}\frac{d}{dt}\left(N_g v_{c,\text{avg}}\right)=ki_{gd}-i_{\text{dc}} \tag{20b}$$

where C_{eq}^{g} is the equivalent arm capacitance of GSC. From (20), the active power P_{ac}^{g} transfer is achieved by controlling the overall average SM capacitor voltage $v_{c,\text{avg}}^{*}$. This voltage controller generates the active power component of the d-axis grid current (i_{gd}^{*}) as illustrated in Fig. 6. For the unity power factor, the reactive power Q_g component of the q-axis grid current i_{gq}^{*} is zero. These reference currents are controlled by the grid current controllers, which generate the converter terminal voltage v_{gsc}^{x*} as shown in Fig. 6. The grid reference position (θ_e) is obtained from PLL. Further, the second harmonic CC controller is implemented to obtain $\Delta v_{\text{gsc}}^{x*}$ [28]. The ac voltage at converter terminals v_{gsc}^{*}, $\Delta v_{\text{gsc}}^{x*}$, and the value of voltage v_{dc}^{*} which is obtained from the current i_{dc} controller, are utilized in (6a) to get the arm voltage v_{ul}^{x} to be generated, as illustrated in Fig. 6. Similar to the MSC, the GSC gate pulses are produced by the PSPWM followed by the sorting and selection algorithm for uniform charge distribution of among SMs within arm.

IV. SIMULATION STUDIES

To substantiate the proposed PHC-drive configuration and control strategy, the simulation model of a three-phase 1.68 MW, 2300 V drive system is developed using PSCAD. The developed model includes the motor side and grid side control strategies which were illustrated in Sections III-A and III-B, respectively. The simulation parameters in SI and per-unit (p.u.) values are tabulated in Table I with base values of 2.1 MW, 2.3 kV, and 527.14 A. Hence, the simulation studies can be extended to the targeted voltages of 11 kV, and 13.8 kV drive systems as well by using the p.u. system.

TABLE I
SPECIFICATIONS OF SIMULATION AND EXPERIMENTAL STUDY

	Simulation		**Experimental**
	SI	***p.u.***	**SI**
Induction motor parameters			
Active power	2.1 MVA	1.0	1.6 kW
Stator LL voltage	2.3 kV	1.0	350 V
Rated current	527.146 A	1.0	3.63 A
Motor speed	1786 rpm	0.992	1455 rpm
Rated torque	8.98 kNm	1.0	10.5 Nm
Rated power factor	0.8	–	0.81
Moment of inertia	63.87 kg-m^2		0.0257 kg-m^2
Pole pairs	2	–	2
PHC operating parameters			
DC-link voltage	3.76 kV	1.635	400 V
Number of HB SMs per CL, N_p	6	–	2
Submodule voltage	314 V	0.136	104.72 V
Number of levels in $v_{s,x}$	13	–	5
SM capacitance	16.67 mF (7 kJ/MVA)		3.3 mF
dc-link inductance	4 mH	0.6	10 mH (4.1%)
Carrier frequency	1000 Hz		1000 Hz
MMC operating parameters			
Grid voltage	2.3 kV	1.0	250 V
No. of FB SMs per arm, N_m	6	–	2
Submodule voltage	733.3 V	0.319	200 V
Number of levels in v_{cnv}	7	–	3
SM capacitance	7.27 mF (33.51 kJ/MVA)	0.14	3.3 *mF*
Grid inductance	0.8018 mH	0.12	10 mH (4.1%)
Arm inductance	0.401 mH	0.06	6 mH (2.5%)
Carrier frequency	1000 Hz	16.67	1000 Hz

In the developed model, six HBSMs and six FBSMs are used in each phase of MSC and GSC, respectively. The simulation studies are conducted at various motor speeds and load torque, including regenerative mode. Initially, the voltage reference (v_c^{p*}) of the overall PHC energy balancing controller, shown in

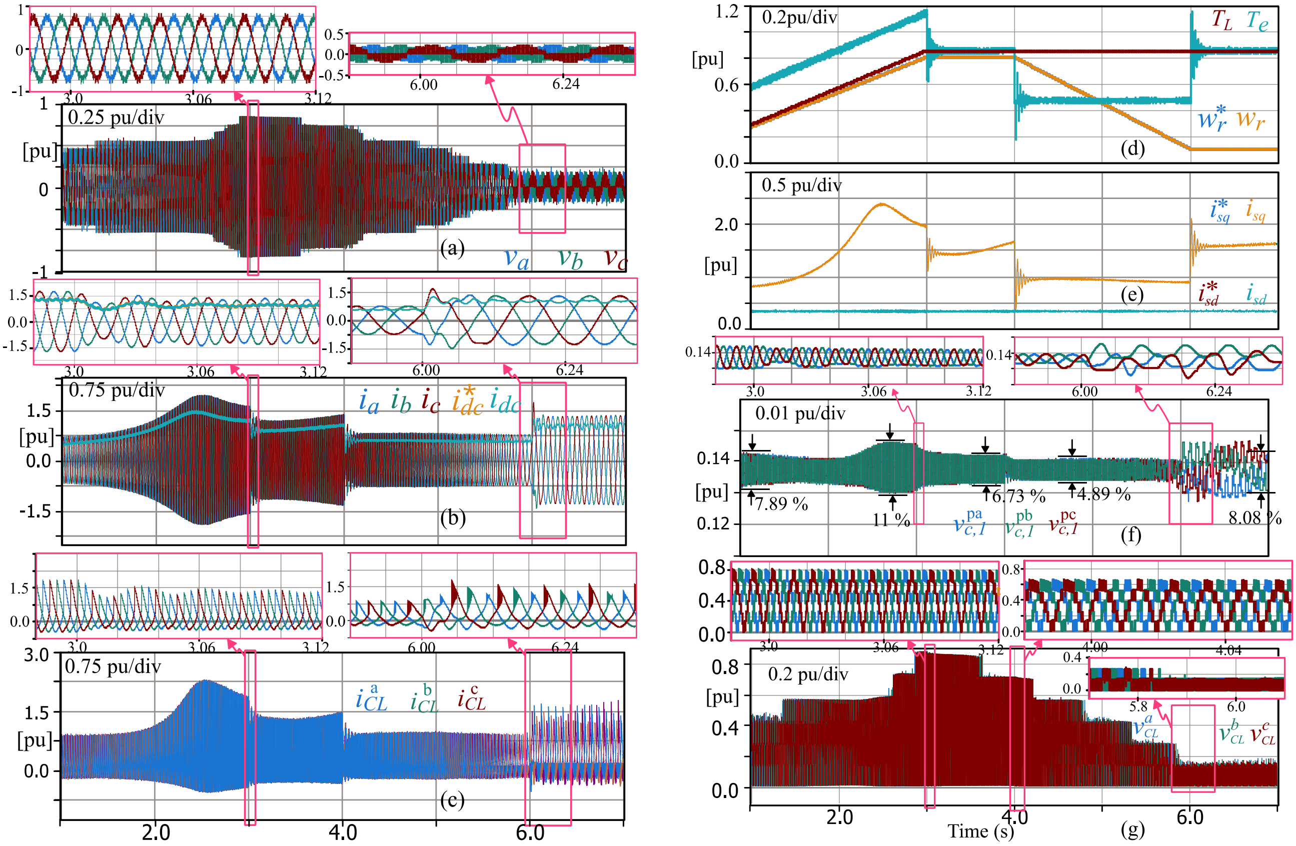

Fig. 7. Simulation waveforms of MSC (motor side), base value: 2.1 MVA, 2.3 kV, 527.14 A: (a) Stator voltages, (b) DC-link current and stator currents, (c) chain-link current, (d) rotor speed and load torque, (e) q-and d-axis stator current, (f) SMs capacitor voltages of MSC, and (g) chain-link voltages.

Fig. 7, is set as $\hat{V}_s/N_p = 1878.1/6 \approx 314$ V. The d-axis current i_{sd}^* responsible for generating the rated flux is calculated and set as 169.42 A. The voltage reference ($v_{c,\text{avg}}^*$) of the GSC energy controller (Fig. 6) is set as $V_{\text{dc}}/N_g = 3760/\,(0.85{*}6) = 733.3$ V. The q-axis current i_{gq}^* is set as zero to obtain the unity-power factor at grid terminals. The PSPWM is utilized for generating gate pulses.

To validate the effectiveness of the proposed drive, the simulation results of the MSC and GSC for various motor speeds and load torque are presented in Figs. 7 and 8, respectively, between the time instants $t = 1$ and 6 s.

A. Operation Between Time t = 1 to 3 s

The speed reference (ω_r^*) and load torque (T_L) are ramped up to 1428.8 rpm (0.8 p.u.) and 7.63 k Nm (0.85 p.u.), respectively, as shown in Fig. 7(d). As ω_r^* increases, the motor voltage v_a and its frequency (f) also increase as directed by vector control of the motor, as in Fig. 7(a). Also, when ω_r has a positive slope, the electrical torque T_e is greater than load torque T_L as shown in Fig. 7(d). The motor side control targets such as speed w_r, and q and d-axis currents (i_{sq} and i_{sd}) are tracking their references as in Fig. 7(e). It can be observed from Fig. 7(b) that the current i_{dc} controller is following the reference current i_{dc}^*, which is generated by the overall energy balancing control of CLs. The current i_{dc} is settled to 453.86 A (0.86 p.u.). The reference v_{dc}^*, obtained from the i_{dc} controller, is established by the GSC. This can be observed from both Fig. 8(f) and through the dc component of the arm voltage (v_u^a or v_l^a), shown in Fig. 7(e).

Thus, there is no dc-link current shoot-through in the proposed drive system while varying the motor speed ω_r. Further, note that i_{dc} is varying proportional to the torque component of the q-axis stator current i_{sq}, as illustrated in Fig. 7(b) and (e). Similarly, the peak value trajectory of CL currents of MSC is proportional to the peak value trajectory of stator currents, shown in Fig. 7(c). Hence, i_{CL}^x fallows (9b). Moreover, the CL currents have a 2ω dominant frequency due to the unfolding H-bridge. This is the main reason for the low energy storage requirement of PHC.

From Fig. 8(g), the active power P_g is steeply raised up to 2.17 MW (1.03 p.u.) and settled to 1.58 MW (0.752 p.u.) while maintaining the zero reactive power Q_g. The voltage v_{dc} would be settled to 1.58 MW/453.86 A = 3481.25 V (1.513 p.u.). The unity power factor operation can also be observed from Fig. 8(a) and (b) throughout the operation while varying the v_{dc}. The amplitude of the grid current $\hat{I}_g$ is steeply raised and settled to 561.18 A (1.06 p.u.), which is proportional to the P_g, as depicted in Fig. 8(b) and (g). The arm currents are shown in Fig. 8(c).

The voltage of the only first SM capacitor of CL or arm is presented due to the uniform distribution of energy among the SMs. From Fig. 7(f), the SMCVs of CLs of MSC $v_{c,1}^{pa}$ are balanced at 314 V (0.136 p.u.) by the overall PHC energy controller, presented in Fig. 6, which is as expected. At 2.7 s,

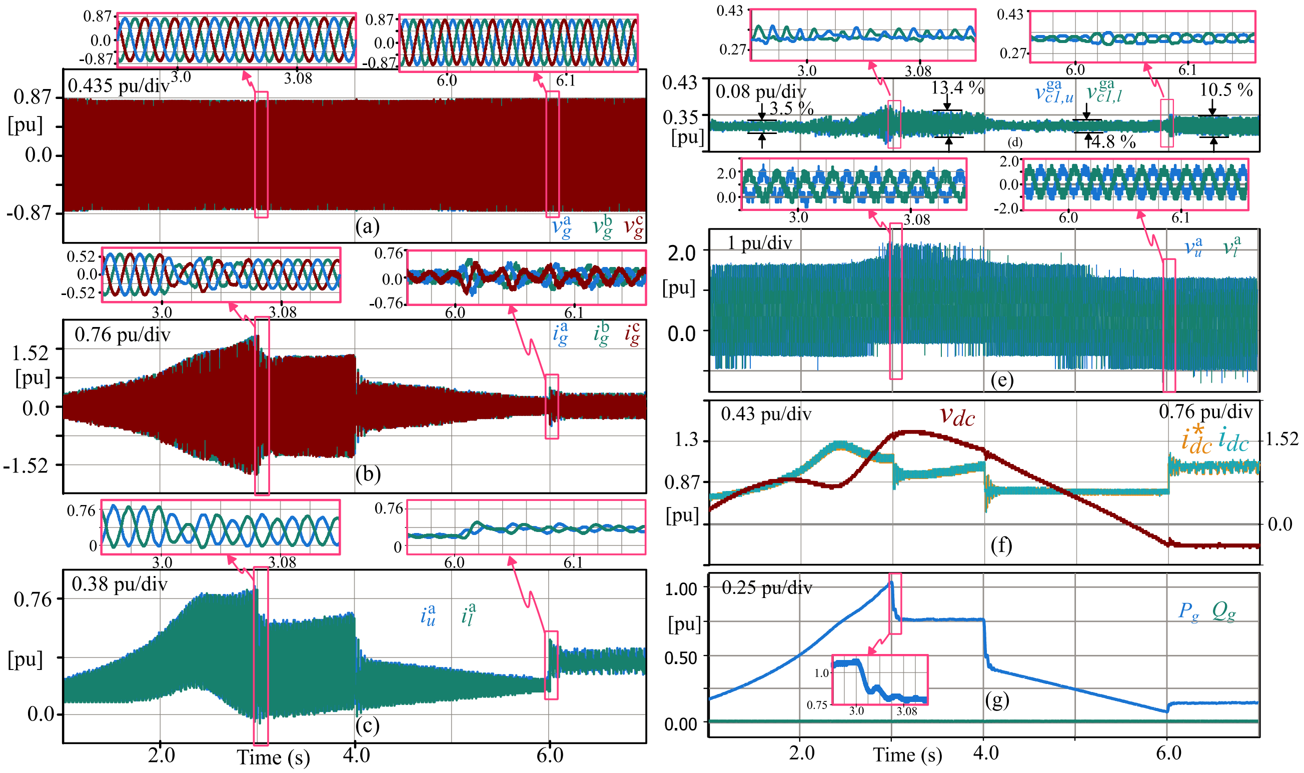

Fig. 8. Simulation waveforms of GSC (grid side), base value: 2.1 MVA, 2.3 kV, and 527.14 A: (a) grid phase voltages, (b) grid currents, (c) arm currents of a-phase, (d) SM_1 capacitor voltage (upper and lower) of GSC, (e) arm voltage (upper and lower), (f) DC-link voltage and current, and (g) grid active and reactive power.

the SMCVR $\Delta V_{c,1}^{pa}$ is 11.03%, which is above the designed ripple (10%) due to the high stator current i_a, as expressed by (11a). Similarly, from Fig. 8(d), the SMCV of GSC $v_{c1,ul}^{ga}$ are balancing at 733.33 V (0.318 p.u.) by the overall capacitor voltage controller (Fig. 7). The CVR $\Delta V_{c1,ul}^{ga}$ is initially 3.5% and finally settled to 13.4% at 0.8 p.u. speed due to the rise of current $\hat{I}_g$ and v_{dc}. This confirms the analytical study in (13a) that the CVR is proportional to i_g and k.

B. *Operation Between Time* t = *3 to 4 s*

In this duration, the reference speed ω_r^* and load torque T_L are constant at 1428.8 rpm (0.8 p.u. speed) and 7.63 kNm (0.85 p.u. torque), respectively as illustrated in Fig. 7(d). Hence, the constant active power P_g of 1.58 MW (0.752 p.u.) is drawing from the grid as shown in Fig. 8(g). The motor side and grid side control targets are following their references, as in Figs. 7 and 8. The amplitude of the stator current i_a is settled to 682.1 A (1.29 p.u.). The SMCVR of MSC $\Delta V_{c,1}^{pa}$ and GSC $\Delta V_{c1,ul}^{ga}$ are 6.73% and 11.1% as in Figs. 7(f) and 8(d), respectively, and are within acceptable limits. This confirms the effectiveness of the proposed drive at high speed and high torque operation.

C. *Operation Between Time* t = *4 to 7 s*

In this duration, the torque remains constant at 7.63 kNm, and the reference speed ω_r^* is ramped down from 1428.8 to 178.6 rpm (0.1 p.u.) and maintained at this low speed to verify the effectiveness of the proposed drive. During ramp down the torque T_e is less than T_L due to the negative slope of the speed ω_r, from Fig. 7(d). The amplitude of the stator current i_a comes down to 414.2 A (0.786 p.u.) during the deceleration and finally settled back to 682.1 A (1.29 p.u.) due to the constant load torque T_L. The control targets of both converters are tracking their references. The amplitude of the CL voltage V_{CL}^{pa} is established proportional to the motor speed as shown in Fig. 7(g). In addition, during deceleration the SMCVR of MSC $\Delta V_{c,1}^{pa}$ is 4.9% and at steady state 8.1%, as shown in Fig. 7(f). Similarly, the SMCVR of GSC $\Delta V_{c1,ul}^{ga}$ is 4.9% during deceleration and 10.5% at steady state, as in Fig. 8(d). Note that this increase in ripple voltage at steady state is due to the increase in amplitude of the stator current or grid current. The CVR reaches its lowest value of 4.8%, and is observed during the 0.5 p.u. speed operation, as evident from Fig. 8. Further, the SMCVR of MSC $\Delta V_{c,1}^{pa}$ is not affected by the operating motor speed.

D. *Regenerative Operation*

To verify the effectiveness of the proposed drive under the regenerative operation the results are presented in Fig. 9. The load torque T_L is positive and constant at 4.49 kNm throughout the operation, as shown in Fig. 9(c). Initially, up to time 2.9 s, the reference speed ω_r^* is maintained at 37.7 rad/s, as in Fig. 9(b), and thus the active power is consumed by the motor. The SMCVs of MSC and GSC are balancing at 314 V (0.136 p.u.) and 733.33 V (0.318 p.u.), respectively. After time 2.9 s, the reference speed ω_r^* is changed to −75.4 rad/s (negative speed). The negative

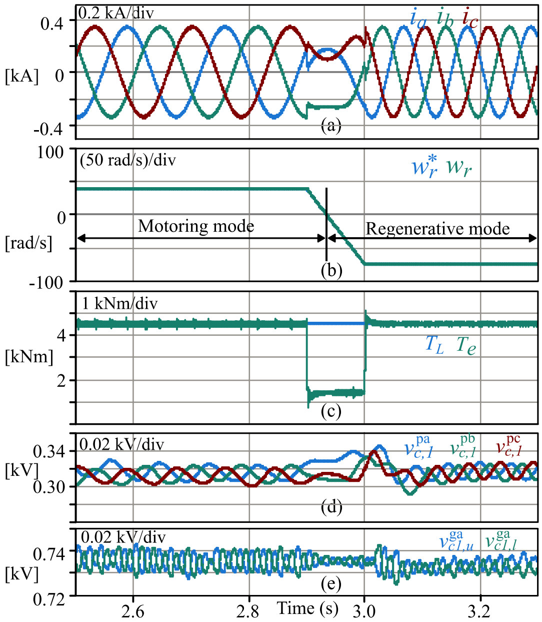

Fig. 9. Simulation waveforms of regenerative operation: (a) stator current, (b) rotor speed, (c) torque, (d) SM capacitor voltage of CLs of MSC, and (d) SM capacitor voltages of arms of GSC.

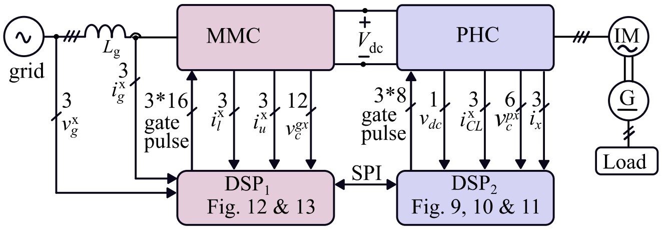

Fig. 10. Schematic of experimental prototype.

power has been generated at the motor, which is evident by the product of ω_r and T_L, i.e., Fig. 9(b) and (c). The corresponding stator current is shown in Fig. 9(a). For both motoring and generating modes, the SMCVs of MSC and GSC are balanced at their reference value, shown in Fig. 9(d) and (e). During the zero-crossing instant of the ω_r the SMCVR of the MSC is raised and settled back to the initial value due to the quick surpassing of the zero instant of the speed. On the other hand, this is not the case for the SMCVR of the GSC due to the rated grid frequency operation.

Hence, the proposed drive is validated at various speeds and load torque for both motoring and regenerating operations.

V. EXPERIMENTAL STUDIES

A scaled-down laboratory prototype is developed to validate the proposed drive configuration and its control strategy. The schematic and photograph of the experimental prototype are shown in Figs. 10 and 11, respectively. They comprise two HBSMs in each CL of PHC and two FBSMs in each arm of the MMC. The IGBTs are utilized to realize the SMs. Two digital signal processors (DSP-TMS320F28335) are used to implement the proposed control strategy, one for each converter.

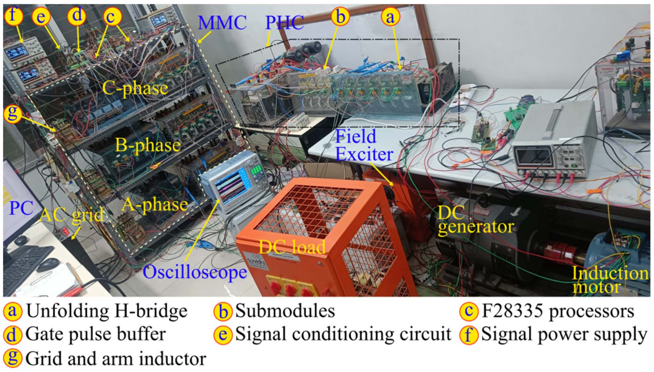

Fig. 11. Photograph of experimental prototype.

The synchronization between them is ensured by using the SPI protocol. The voltages and currents are sensed using sensing boards and channeled to respective DSPs via signal conditioning board. At every 50 μs of time interval, the time-critical tasks such as current control and capacitor voltage balancing algorithms are implemented. The GSC control (Fig. 6) is implemented in DSP$_1$. The MSC control (Fig. 4) is implemented in DSP$_2$. The v/f speed control is implemented, and the induction motor is electrically loaded using the dc generator. The Yokogawa DL850E ScopeCorder is used for measuring and storing experimental results. The parameters of PHC, MMC, and induction motor are given in Table I.

The performance of the proposed drive configuration and control strategy is studied at high-speed and low-speed operations, dynamic load change, and regenerative operation using this experimental prototype. Initially, the motor is under no load condition and the PLL is locked to the voltage v_g. For the rated voltage $V_{\text{dc}}^{\text{rated}}$ of 400 V the SMCV reference of MSC v_c^* is set as $v_{\text{dc}} \times \pi/(6N_p) = 400\pi/(6 \times 2) = 104.72$ V. The SMCV reference of GSC $v_{c,\text{avg}}^*$ is set as $v_{\text{dc}}/N_g = 400/2 = 200$ V. In the experiment, the required amplitude of the grid voltage $\hat{V}_g^x$ is 160 V to obtain the v_{dc} of 400 V. The experiment results for high speed and low speed are presented in Figs. 12 and 13, respectively.

A. Operation at 1 p.u. Speed

Fig. 12 shows the various waveforms such as stator voltage v_g^x and current i_g^x of the proposed drive configuration at 1 p.u. speed ω (50 Hz frequency). The voltage v_{dc} of 392 V is observed from Fig. 12(i). The load of 1.15 kW is applied on the motor using the dc generator. The amplitude of the stator current i_x is 5 A as shown in Fig. 12(b). The current i_{dc} can be calculated as $p_{\text{dc}}/v_{\text{dc}}$ $= 1150/392 = 2.93$ A. This i_{dc} can be observed from Fig. 12(j) due to the dc-link controller. The SMCVs $v_{c,1}^{pa}$ of CL of MSC are balanced at 103 V as shown in Fig. 12(e) due to the overall energy balancing control of CLs. As the number of SMs $N_p = 2$ is used in a CL the amplitude of the CL voltages v_{CL}^x would be 206 V as in Fig. 12(d). The voltage v_{CL}^x waveforms are unfolded using the H-bridge to obtain stator voltage v_x as in Fig. 12(a). The voltage v_x waveforms have five (=$2N_p$+1) levels. The CL currents i_{CL}^x follow (9a) and have 100 Hz (2ω) frequency due to

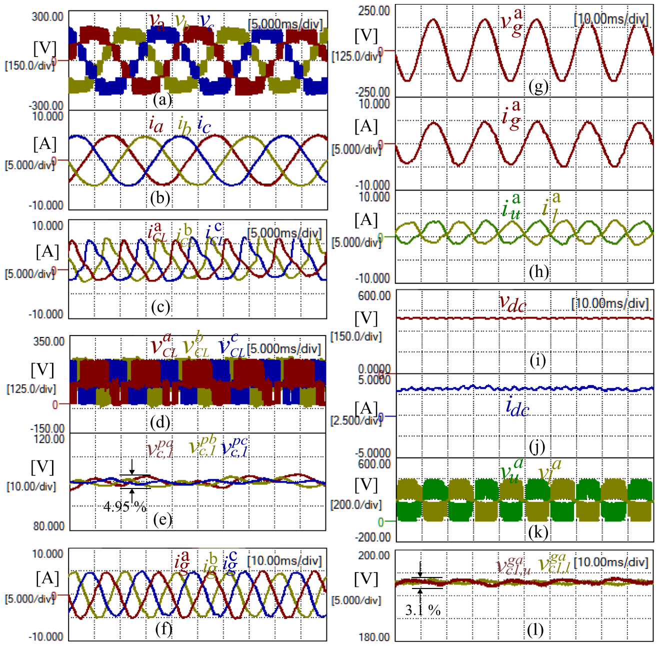

Fig. 12. Experimental waveforms at 1.0 p.u. speed (50 Hz) MSC: (a) stator voltage, (b) stator currents, (c) CL currents, (d) CL voltages, and (e) SM$_1$ capacitor voltage of each CL; GSC: (f) grid currents, (g) grid voltage, (h) arm currents, (i) DC-link voltage, (j) DC-link current, (k) arm voltages, and (l) SM$_1$ capacitor voltages of upper and lower arm.

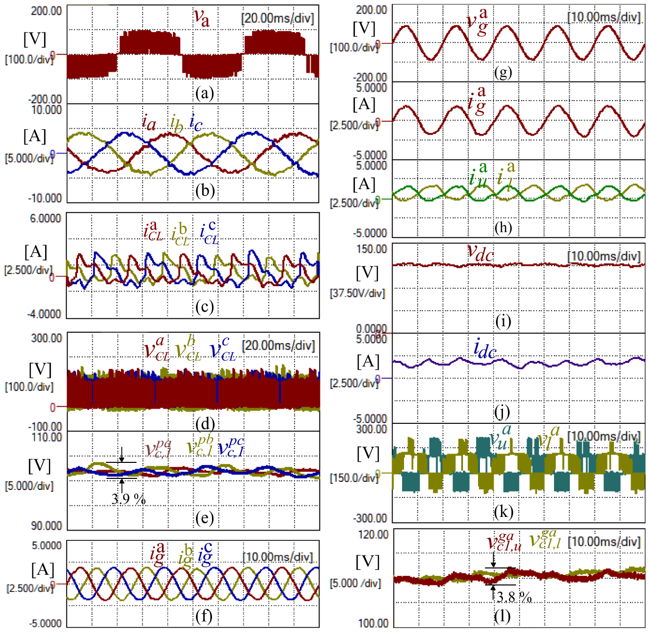

Fig. 13. Experimental waveforms at 0.2 p.u. speed (10 Hz) MSC: (a) stator voltage, (b) stator currents, (c) CL currents, (d) CL voltages, and (e) SM$_1$ capacitor voltage of each CL; GSC: (f) grid currents, (g) grid voltage, (h) arm currents, (i) DC-link voltage, (j) DC-link current, (k) arm voltages, and (l) SM$_1$ capacitor voltages of upper and lower arm.

the unfolding H-bridge, shown in Fig. 12(c). This 2ω component helps to reduce the SMCVR. From Fig. 12(e), the CLs SMCVR $\Delta V^{pa}_{c,1}$ is 5 V (4.95%). The voltage $v_{\rm dc}$, as shown in Fig. 12(i), is generated by the GSC converter. The grid voltage v^x_g and currents i^x_g are shown in Fig. 12(g) and (f), respectively. The unity power factor of the grid is evident from Fig. 12(g). The amplitude of the current i^x_g is calculated as $P_g/(\hat{V}^x_g \times 3/2) = 1150/(160 \times 3/2) = 4.79$ A and can be observed from Fig. 12(f). The arm currents of GSC are shown in Fig. 12(h). The SMCVs of GSC $v^{ga}_{c,1}$ are balancing at 192 V, as shown in Fig. 12(l). The SMCVR $\Delta V^{ga}_{c1,ul}$ is 6 V (3.1%) as shown in Fig. 12(l). The arm voltages v^a_u and v^a_l of GSC are as shown in Fig. 12(k). Due to the rated dc-link voltage ($k = 1$), the number of negatively inserted SMs in v^a_u are zero ($M = 0$).

B. Operation at 0.2 p.u. Speed

The motor is operated at 0.2 p.u. speed ω (10 Hz operating frequency) using experimental prototype. The required dc-link voltage ($v_{\rm dc}$) would be $393 \times 0.2 = 79$ V. Due to the nonlinearity during low-speed operation the $v_{\rm dc}$ is required as 112 V. The SMs average capacitor voltage reference $v^*_{c,\rm avg}$ of GSC is chosen as 110 V, while the SM capacitor voltage reference of MSC v^*_c is 103 V which is the same as the earlier operation. Various waveforms of the MSC and GSC are shown in Fig. 13. The motor is loaded with 225 W of power. The amplitude of the stator current (i_x) is 4 A (80% of the amplitude of rated i_x) as shown in Fig. 13(b). The corresponding CL currents of MSC are given in Fig. 13(c). The current $i_{\rm dc}$ can be calculated to be as $p_{\rm dc}/\, v_{\rm dc} = 225/112 = 2$ A. This $i_{\rm dc}$ can be observed from Fig. 13(j) due to the dc-link controller. The SMCV of CL of MSC $v^{pa}_{c,1}$ is balanced at 103 V, shown in Fig. 13(e). The SMCVR of CL of MSC is 4 V (3.9%). It can be noticed that the SM capacitor ripple voltages of MSC $v^{pa}_{c,1}$ are not affected by the operating motor speed.

The amplitude of the grid voltage v^x_g is 80 V as shown in Fig. 13(e). The amplitude of the grid current i^x_g is calculated as $P_g/(\hat{V}^x_g \times 3/2) = 225/(80 \times 3/2) = 1.87$ A. This can be observed from Fig. 13(f). The arm currents of GSC are shown in Fig. 13(h). The SMCVs of GSC $v^{ga}_{c,1}$ are balancing at 110 V, as shown in Fig. 13(l). The SMCVR is 6 V (5.4%) as shown in Fig. 13(l). The arm voltages v^a_u and v^a_l of GSC are as shown in Fig. 13(k). The fraction of the dc-link voltage (k) is $112/(2 \times 110) = 0.51$). So the negatively inserted arm voltages v^a_u and v^a_l can be observed in Fig. 13(k).

C. Dynamic Performance During Load Change

In Fig. 14, the experimental results of the dynamic performance of the proposed configuration are demonstrated. Initially, the motor operated with 0.3 kW at 1160 rpm for the duration of t_1 to t_2. The corresponding frequency and amplitude of the stator current are 40 Hz and 1.2 A, as in Fig. 14(a). The SMCVs of PHC are controlled at their reference value of 102 V, and their ripple is 3 V (3%), shown in Fig. 14(b). The SMCVs of MMC are controlled at their reference value of 192 V, and their ripple is 5 V (2.6%), shown in Fig. 14(c). At time t_2, a sudden load of 0.68 kW is applied to the motor. The corresponding amplitude of the motor current rises to 3.8 A, from Fig. 14(a). The SMCVs of PHC decreased to 92 V due to the sudden load and eventually settled back to their reference value of 102 V with its ripple of 4.3 V (4.2%) (during t_2 to t_3). Similarly, the SMCVs of MMC are settled to their reference value of 192 V due to the voltage controller for the active power component, shown in Fig. 14(c).

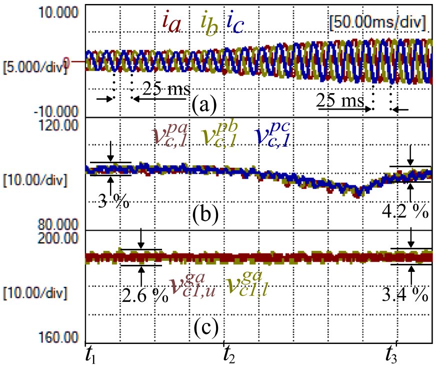

Fig. 14. Experimental dynamic performance results during load change: (a) stator currents, (b) SMs capacitor voltage of MSC, and (c) SMs capacitor voltage of GSC.

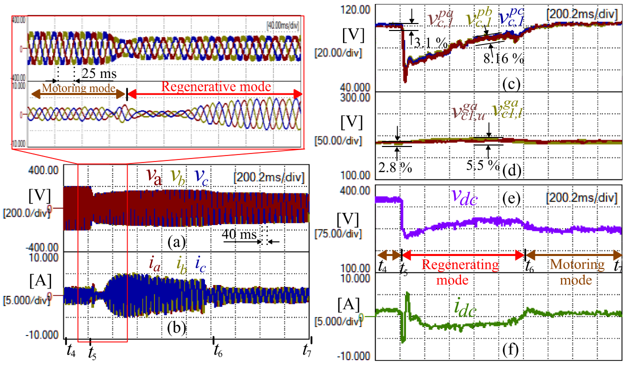

Fig. 15. Experimental waveforms of regenerative operation: (a) stator voltages, (b) stator currents, (c) SMs capacitor voltage of MSC, (d) SMs capacitor voltage of GSC, (e) DC-link voltage, and (f) DC-link current.

The corresponding voltage ripple is 6.5 V (3.4%). It can be observed that the increase in SMCVR is due to the increase in load current.

D. Regenerative Operation

The experimental regenerative operation of the proposed work is demonstrated in Fig. 15. From time t_4 to t_5, the drive is in the motoring mode where the amplitude and frequency of stator current are 2 A and 40 Hz, respectively. The motor speed is 242.95 rad/s (electrical). The SMCV of the PHC is 100 V, and its ripple is 3.1 V (3.1%), shown in Fig. 15(c). The corresponding dc-link voltage generated by the MMC is 340 V. The SMCV of MMC and its ripple are 190 and 5.3 V (2.8%), respectively, shown in Fig. 15(d). To demonstrate the regenerative mode, at time t_5, the operating frequency is step-changed from 40 to 25 Hz. So the stator field will rotate at 157.08 rad/s. Since the motor speed is greater than the stator field speed, the motor feeds its stored kinetic energy back to the grid. This can be observed from the negative direction of the stator current and the dc-link current during time t_5 to t_6 in Fig. 15(b) and (f), respectively. In this duration, SMCVs of PHC are settled back to their reference value of 100 V due to the voltage balancing controller, and their ripple is 8.16 V (8.16%). This rise in voltage ripple is due to the increased stator current. The corresponding SMCV and its ripple of MMC are 190 and 10.5 V (5.5%). The increase in ripple voltage is due to the increased stator current and operating frequency. The generated dc-link voltage by the MMC is changed from 340 to 250 V as directed by the dc-link current controller. When the stored energy is depleted at t_6, the drive returns to motoring mode, resuming rotation at a speed of 157.08 rad/s.

VI. COMPARATIVE ANALYSIS OF THE PROPOSED DRIVE

This section presents a comparative analysis of the proposed drive over state-of-the-art MMC-based drives, as illustrated in Table II, to evaluate its advantages and disadvantages. For fair comparison, all drives are assessed under identical parameters, including voltages $\hat{V}_m$ and V_{dc}, currents $\hat{I}_m$ and $\hat{I}_g$, number of phase voltage levels $(N+1)$, apparent power (S), and the voltage-stress per device (V_{dc}/N) is considered same across all these drives. The total components count comprising IGBTs, diodes, and capacitors is a useful indicator for assessing system reliability. From Table II, AFE–CHB has the least component requirement of $16.5N$, and least energy storage requirement (8.21 kJ/MVA) among all the considered configurations as well as the proposed drive. However, this comes at the cost of complex multiwinding phase-shifting transformer, harmonic filters [33], which leads to high weight, volume, and initial/operating cost, from Table II. Also, it has complexity in providing redundant modules, affects grid harmonic performance due to phase-shift deviations [33].

Further, the proposed drive requires $(34.5N + 36)$ number of 6500 V IGBTs, and capacitive energy storage of 36.31 kJ/MVA. In regenerative MMC-based drives, the total components count is $60N$ in MMC–MMC drive [20], $42N$ in hybrid MMC drive [44], $48N$ in magnetic CL MMC drive [48] and $37N$ in delta-channel MMC drive [47] as tabulated in Table II. Hence, the proposed drive needs the least number of components among the regenerative MMC-based drives.

In nonregenerative drives, the components required are $24N$ in the DFE–MMC [34], $33N$ in the AC–MMC [19], $27N$ in the FC–MMC [41], and $31.5N$ in the star-channel MMC-based drives [46], [47]. Hence, compared to the proposed drive, other systems like the DFE–MMC, AC–MMC, FC–MMC, and star-channel MMC-based drives require fewer components. However, these alternatives are nonregenerative and rely on standard transformers for 24-pulse rectifiers, high bandwidth controller for CC and CMV [19]. Also, the FC–MMC drive requires series connection of capacitors, and their precharging and balancing mechanism [41].

Additionally, from Table II, the proposed drive features the least number of capacitors $(7.5N)$ among the regenerative MMC-based drives [19], [41], [46], [47], [48]. Consequently, the AFE–CHB drive exhibits the lowest capacitive energy storage requirement at 8.21 kJ/MVA, followed by the proposed drive at 36.31 kJ/MVA, which is still lower than that of all other regenerative and nonregenerative MMC-based drives as shown in Fig. 16, which is in p.u. MVA, hence, independent of voltage rating of drive system.

Fig. 17 illustrates components count for the 6.9 and 13.8 kV drive systems, derived from Table II, where the phase voltage

TABLE II
COMPARISON OF PROPOSED CONFIGURATION WITH EXISTING STATE-OF-THE-ART MV DRIVES

Parameters		**CHB [33]**	**DFE–MMC [34]**	**AC–MMC [19]**	**FC–MMC [41]**	**Star-channel MMC [46]**	**Delta-channel MMC [47]**	**Magnetic chain-link MMC [48]**	**MMC–MMC [20]**	**Hybrid MMC with series switch [43]**	**Hybrid BTB MMC**		**MMC–PHC (proposed)**
											[44]	**[45]**	
DC-link voltage		$0.5V_{dc}$	V_{dc}	V_{dc}	V_{dc}	V_{dc}	V_{dc}	V_{dc}	V_{dc}	V_{dc}	V_{dc}	V_{dc}	V_{dc}
No. of isolated dc sources		$3N/2$	1	1	1	1	1	1	1	1	1	1	1
Levels in output phase voltage		$N+1$	$N+1$	$N+1$	$N+1$	$N+1$	$N+1$	$N+1$	$N+1$	$N+1$	$N+1$	$N+1$	$N+1$
Voltage stress per device		V_{dc}/N	V_{dc}/N	V_{dc}/N	V_{dc}/N	V_{dc}/N	V_{dc}/N	V_{dc}/N	V_{dc}/N	V_{dc}/N	V_{dc}/N	V_{dc}/N	V_{dc}/N
No. of submodules	Grid side	$3N/2$	–	–	–	–	–	–	$6N$	–	$6N$	$6N$	$6N$
	Motor side	$3N/2$	$6N$	9N	6N	$(6+0.25)N$	$(6+0.25\sqrt{3})N$	6N	$6N$	6N	$6N$	$6N$	$3N/2$
Device current rating	Grid side	$\hat{I}_g$	$\hat{I}_g$	$\hat{I}_g$	$\hat{I}_g$	$\hat{I}_g$	$\hat{I}_g$	$\hat{I}_g$	$0.75\hat{I}_g$	$\hat{I}_g$	$\hat{I}_g$	$0.75\hat{I}_g$	$0.75\hat{I}_g$
	Motor side	$\hat{I}_m$	$0.75\hat{I}_m$	$0.75\hat{I}_m$	$0.75\hat{I}_m$	$0.75\hat{I}_m$	$0.75\hat{I}_m$	$0.75\hat{I}_m$	$0.75\hat{I}_m$	$0.75\hat{I}_m$	$0.75\hat{I}_m$	$0.75\hat{I}_m$	$\hat{I}_m$
No. of devices	Diodes	DFE: $9N$ AFE: -	$6N$	$6N$	$6N$	$6N$	$6N$	$6N$	-0	$6N$	–	–	–
	IGBTs	DFE: $6N$ AFE: $15N$	$12N$	$18N$	$12N$	$18N$	$22.4N$	$36N$	$48N$	IGBT:$12N$ Thyristor: N	$30N$	$30N$	$27N+$ 36 HV-IGBTs
No. of capacitors		$1.5N$	$6N$	$9N$	$9N$	$7.5N$	$8.6N$	$6N$	$12N$	$6N$	$12N$	$12N$	$7.5N$
Capacitive energy (kJ/MVA)		8.21	265.2	104.5	73.1	87.11	99.89	134.32	55.33	47	55.33	132.1	36.31
No. of inductors		No	6	12	12	6	12	6	12	6	12	12	7
Transformer (T/F) rating and type		1 pu (complex)	1 pu (24-pulse)	1 pu (24-pulse)	1 pu (24-pulse)	1 pu (24-pulse)	1 pu (24-pulse)	1 pu (24-pulse)	No	1 pu (24-pulse)	No	No	No
Need for high BW control on MSC		dedicated SM cap. balance	Yes	Yes	Yes	Yes	Yes	Yes	Yes	Yes	Yes	Yes	No
Need of device series connection		No	No	No	Yes	No	No	No	No	No	No	No	Yes (up to 2 or 3)
Regenerative energy savings		DFE: No AFE: Yes	No	No	No	No	No	No	Yes	No	Yes	Yes	Yes

$V_{dc}(=2V_m)$: dc-link voltage, $\hat{I}_m$: motor's peak phase current, $\hat{I}_g$: grid's peak phase current, $N+1$: no., of levels in phase voltage

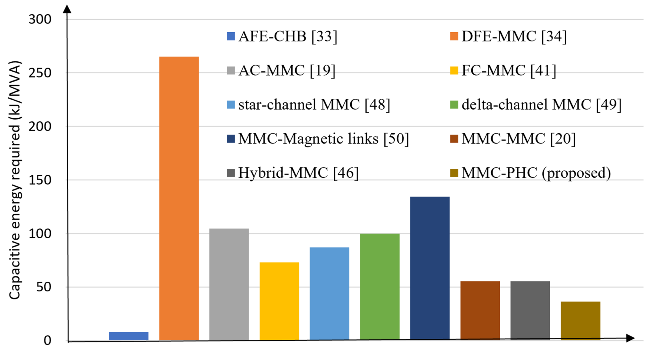

Fig. 16. Comparison of capacitive energy storage of MMC-based drives.

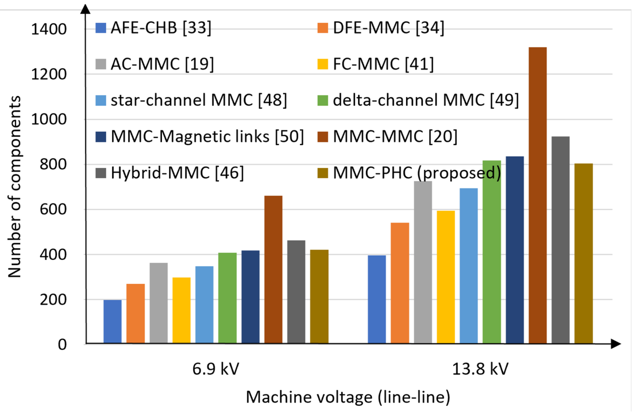

Fig. 17. Comparison of number of components of MMC-based drives.

levels are 12 and 23 in 6.9 kV and 13.8 kV, respectively. In this context, each semiconductor device experiences a voltage stress of 1 kV, and each switch in the unfolding H-bridge of the proposed drive consists of three series-connected 6.5 kV IGBTs. As shown in Fig. 17, the AFE–CHB drive has the lowest overall components count, while the MMC–MMC drive has the highest, followed by the hybrid MMC drive [44], MMC with magnetic links [48], delta channel MMC [47], and the proposed drive in both 6.9 and 13.8 kV drive systems, as discussed earlier. Further, compared to the proposed drive, other drives like the DFE–MMC [34], AC–MMC [19], FC–MMC [41], and star channel MMC-based drives [46], [47] require fewer components as in Table II.

Moreover, the injection of HF voltage and/or current in MSC is essential to balance SMCVs in all the examined drives, potentially requiring high bandwidth controllers [33], [34], [43], [44], [45], [46], [47], [48]. Conversely, in the case of MSC, the proposed drive injection of HF components is not necessary, thereby reducing control complexity. Additionally, the proposed drive operates without a transformer, resulting in a reduced system footprint, lower weight, and simplified structure. Despite a modest increase in submodules count, the proposed configuration achieves full regeneration capability and improved integration potential for medium-voltage high-power applications. Hence, the proposed transformerless drive configuration offers a balanced tradeoff between regenerative operation, control complexity, and components count.

VII. CONCLUSION

In this article, a transformerless MMC–PHC drive configuration is proposed to address the dc-link current shoot-through problem associated with variable-speed operation in PHC-based OEWM drives. The FBSMs-based MMC on the grid side synthesizes the variable dc-link voltage while maintaining the active and reactive power control at the grid interface. This variable dc-link voltage enables the PHC to achieve variable-speed operation through the proposed drive configuration and its control algorithm. Also, the SMCVR of the GSC and MSC remains unaffected by the operating speed. The proposed drive eliminates the need for a substantial CC injection and CMV injection requirement in MMC drive. Additionally, the proposed drive achieves significant energy storage reduction, requiring only 36.31 kJ/MVA compared to 55.33 kJ/MVA in the existing MMC–MMC and hybrid-MMC drives. The design of the dc-link inductor remains unaffected by the variable voltage and frequency operation of the PHC drive. The proposed control strategy has ensured the balancing of SMCVs of MMC and PHC under high-speed and low-speed operations, dynamic load changes, and regenerative operations, as validated through simulation and experimental studies. Furthermore, the natural ZVS operation in the unfolding H-bridge of the PHC simplifies the complexity of series-connected devices compared to conventional MV drives. Despite a modest increase in submodules count compared to nonregenerative MMC drives, the proposed configuration offers a balanced tradeoff between regenerative operation, control complexity, and components count. So the proposed transformerless MMC–PHC drive would be a promising solution for high-power VSDs due to its reduced energy storage requirements, modular structure, and capability for regenerative operation.

REFERENCES

[1] G. F. Gontijo, T. Kerekes, D. Sera, M. Ricco, L. Mathe, and R. Teodorescu, "New converter solution with a compact modular multilevel structure suitable for high-power medium-voltage wind turbines," *IEEE Trans. Power Electron.*, vol. 38, no. 2, pp. 2626–2645, Feb. 2023.

[2] P H., P. Pandey, J. Titus, and K. Hatua, "A 12-pulse LCI- and VSI-fed hybrid medium-voltage drive for an induction motor with a tapped split-phase stator winding," *IEEE Trans. Power Electron.*, vol. 39, no. 1, pp. 1230–1243, Jan. 2024.

[3] A. H. Abuelnaga, Z. Ni, S. Badawi, M. Narimani, A. Sayed-Ahmed, and N. R. Zargari, "A new active front-end control for regenerative cascaded H-bridge motor drives with filter- less interfacing capability," *IEEE Trans. Power Electron.*, vol. 38, no. 7, pp. 8559–8570, Jul. 2023.

[4] M. J. Cheerangal, A. K. Jain, and A. Das, "Multiple fault tolerant control strategy for rotor field oriented induction motor drive fed from CHB converter with redundant cells," *IEEE Trans. Power Electron.*, vol. 38, no. 1, pp. 852–861, Jan. 2023.

[5] S. Du, Q. Song, and J. Liu, "A novel modular magnetic-coupled converter (MMCC) for medium-voltage motor drive with minimized DC capacitance and transformer volume," *IEEE Trans. Power Electron.*, vol. 39, no. 2, pp. 2448–2457, Feb. 2024.

[6] F. Deng, J. Hou, Y. Zhang, M. Cheng, Y. Hu, and S. Vazquez, "A furtherance of high-power adjustable-speed drive systems: Medium-frequency ac link-powered machine drive systems," *IEEE Ind. Electron. Mag.*, vol. 17, no. 4, pp. 17–31, Dec. 2023.

[7] J. W. Zapata, G. Postiglione, D. Falchi, G. Borghetti, T. A. Meynard, and G. Gateau, "Multilevel converter for 4.16- and 6.6-kV variable speed drives," *IEEE Trans. Power Electron.*, vol. 36, no. 3, pp. 3172–3180, Mar. 2021.

[8] Y. Okazaki et al., "Experimental comparisons between modular multilevel DSCC inverters and TSBC converters for medium-voltage motor drives," *IEEE Trans. Power Electron.*, vol. 32, no. 3, pp. 1805–1817, Mar. 2017.

[9] A. Antonopoulos, L. Ängquist, L. Harnefors, and H. P. Nee, "Optimal selection of the average capacitor voltage for variable-speed drives with modular multilevel converters," *IEEE Trans. Power Electron.*, vol. 30, no. 1, pp. 227–234, Jan. 2015.

[10] S. Sau and B. G. Fernandes, "Modular multilevel converter based variable speed drive with reduced capacitor ripple voltage," *Trans. Ind. Electron.*, vol. 66, no. 5, pp. 3412–3421, 2019.

[11] M. Basic, M. Utvic, and D. Dujic, "Hybrid modular multilevel converter design and control for variable speed pumped hydro storage plants," *IEEE Access*, vol. 9, pp. 140050–140065, 2021.

[12] M. A. Perez, S. Bernet, J. Rodriguez, S. Kouro, and R. Lizana, "Circuit topologies, modeling, control schemes, and applications of modular multilevel converters," *IEEE Trans. Power Electron.*, vol. 30, no. 1, pp. 4–17, Jan. 2015.

[13] "M2L series medium voltage variable frequency drive 2.3 kV class - 7.2 KV class," Benshaw, 2020. Accessed: Dec. 1, 2023. [Online]. Available: https://benshaw.com/wp-content/uploads/2020/01/benshaw-m2l-3000-brochure.pdf

[14] "SINAMICS PERFECT HARMONY GH150—optimum drive for applications in the medium voltage range 4–13.8 kV," Siemens, 2023. Accessed: Dec. 01, 2023. [Online]. Available: https://www.innomotics.com/en/products/converters/medium-voltage-converters/sinamics-perfect-harmony-gh150.html

[15] J. Kolb, F. Kammerer, M. Gommeringer, and M. Braun, "Cascaded control system of the modular multilevel converter for feeding variable-speed drives," *IEEE Trans. Power Electron.*, vol. 30, no. 1, pp. 349–357, Jan. 2015.

[16] B. Li et al., "An improved circulating current injection method for modular multilevel converters in variable-speed drives," *IEEE Trans. Ind. Electron.*, vol. 63, no. 11, pp. 7215–7225, Nov. 2016.

[17] L. He, K. Zhang, J. Xiong, S. Fan, and Y. Xue, "Low-frequency ripple suppression for medium-voltage drives using modular multilevel converter with full-bridge submodules," *IEEE J. Emerg. Sel. Top. Power Electron.*, vol. 4, no. 2, pp. 657–667, Jun. 2016.

[18] Y. Okazaki, M. Hagiwara, and H. Akagi, "Start-up and low-speed operation of an electric motor driven by a modular multilevel cascade inverter," *IEEE Trans. Ind. Appl.*, vol. 49, no. 4, pp. 1556–1566, Jul./Aug. 2013.

[19] S. Du, B. Wu, K. Tian, N. R. Zargari, and Z. Cheng, "An active cross-connected modular multilevel converter (AC-MMC) for a medium-voltage motor drive," *IEEE Trans. Ind. Electron.*, vol. 63, no. 8, pp. 4707–4717, Aug. 2016.

[20] Y. S. Kumar and G. Poddar, "Medium-voltage vector control induction motor drive at zero frequency using modular multilevel converter," *IEEE Trans. Ind. Electron.*, vol. 65, no. 1, pp. 125–132, Jan. 2018.

[21] Y. Zhang, F. Deng, P. Li, and J. Zhang, "Extended frequency range operation for cascaded MMC and cycloconverter based machine drive system," *IEEE Trans. Power Electron.*, vol. 39, no. 2, pp. 2608–2619, Feb. 2024.

[22] F. Zhao, G. Xiao, T. Zhu, X. Zheng, Z. Wu, and T. Zhao, "A coordinated strategy of low-speed and start-up operation for medium-voltage variable-speed drives with a modular multilevel converter," *IEEE Trans. Power Electron.*, vol. 35, no. 1, pp. 709–724, Jan. 2020.

[23] M. S. Diab, A. M. Massoud, S. Ahmed, and B. W. Williams, "A dual modular multilevel converter with high-frequency magnetic links between submodules for MV open-end stator winding machine drives," *IEEE Trans. Power Electron.*, vol. 33, no. 6, pp. 5142–5159, Jun. 2018.

[24] R. Feldman et al., "A hybrid modular multilevel voltage source converter for HVDC power transmission," *IEEE Trans. Ind. Appl.*, vol. 49, no. 4, pp. 1577–1588, Jul./Aug. 2013.

[25] I. C. Rath, S. K. Patro, and A. Shukla, "Parallel-hybrid converter based STATCOM: Operating principles and capacitor voltage control using fundamental frequency zero-sequence voltage," *IEEE Trans. Power Electron.*, vol. 37, no. 10, pp. 12134–12150, Oct. 2022.

[26] N. R. Karaka, I. C. Rath, and A. Shukla, "Parallel hybrid converter-based adjustable speed drives using third harmonic voltage injection technique," in *Proc. 25th Eur. Conf. Pow. Electron. Appl.*, 2023, pp. 1–8.

[27] J. Chivite-Zabalza, D. R. Trainer, J. C. Nicholls, and C. C. Davidson, "Balancing algorithm for a self-powered high-voltage switch using series-connected IGBTs for HVDC applications," *IEEE Trans. Power Electron.*, vol. 34, no. 9, pp. 8481–8490, Sep. 2019.

[28] K. Sharifabadi, L. Harnefors, H. P. Nee, S. Norrga, and R. Teodorescu, *Design, Control and Application of Modular Multilevel Converters for HVDC Transmission Systems*. Hoboken, NJ, USA: Wiley-IEEE Press, 2016.

[29] M. H. Rashid, *Power Electronics Handbook*, 4th ed. Butterworth-Heinemann, Oxford, U.K., 2017, pp. 252–285.

[30] N. Z. Du, Sixing, A. Dekka, and B. Wu, *Modular Multilevel Converters: Analysis, Control, and Applications*. Hoboken, NJ, USA: Wiley, 2018.

[31] S. Debnath, J. Qin, and M. Saeedifard, "Control and stability analysis of modular multilevel converter under low-frequency operation," *IEEE Trans. Ind. Electron.*, vol. 62, no. 9, pp. 5329–5339, Sep. 2015.

[32] H. Akagi, S. Inoue, and T. Yoshii, "Control and performance of a transformerless cascade PWM STATCOM with star configuration," *IEEE Trans. Ind. Appl.*, vol. 43, no. 4, pp. 1041–1049, Jul./Aug. 2007.

[33] Z. Ni et al., "A new approach to input filter design for regenerative cascaded H-bridge drives," *IEEE Trans. Ind. Electron.*, vol. 69, no. 4, pp. 3266–3277, Apr. 2022.

[34] M. Hagiwara and H. Akagi, "Control and experiment of pulsewidth-modulated modular multilevel converters," *IEEE Trans. Power Electron.*, vol. 24, no. 7, pp. 1737–1746, Jul. 2009.

[35] ABB, "HVDC light & SVC light projects worldwide," ABB Grid Systems-HVDC, Ludvika, Sweden, Tech. Rep. POW-0027, May 2012. Accessed: Feb. 21, 2024. [Online]. Available: https://new.abb.com/docs/default-source/ewea-doc/hvdc-light-and-svc.pdf?sfvrsn=2

[36] ABB, "ACS1000 Flexible and reliable medium-voltage drive," ABB medium-voltage AC drives. Accessed: Dec. 13, 2024. [Online]. Available: https://new.abb.com/drives/medium-voltage-ac-drives/acs1000

[37] Innomotics, "Mediumvoltage converter SM150," Innomotics medium-voltage drives, Innomotics GmbH, Nuremberg, Germany. Accessed Dec. 13, 2024. [Online]. Available: https://www.innomotics.com/hub/en/portfolio/products/medium-voltage-drives/sm150

[38] N. Flourentzou, V. G. Agelidis, and G. D. Demetriades, "VSC-based HVDC power transmission systems: An overview," *IEEE Trans. Pow. Electron*, vol. 24, no. 3, pp. 592–602, Mar. 2009.

[39] P. K. Steimer, H. E. Gruning, J. Werninger, E. Carroll, S. Klaka, and S. Linder, "IGCT—A new emerging technology for high power, low cost inverters," *IEEE Ind. Appl. Mag.*, vol. 5, no. 4, pp. 12–18, Jul./Aug. 1999.

[40] J. Rodriguez, S. Bernet, B. Wu, J. O. Pontt, and S. Kouro, "Multilevel voltage-source-converter topologies for industrial medium-voltage drives," *IEEE Trans. Ind. Electron.*, vol. 54, no. 6, pp. 2930–2945, Dec. 2007.

[41] S. Du, B. Wu, N. R. Zargari, and Z. Cheng, "A flying-capacitor modular multilevel converter for medium-voltage motor drive," *IEEE Trans. Power Electron.*, vol. 32, no. 3, pp. 2081–2089, Mar. 2017, doi: 10.1109/TPEL.2016.2565510.

[42] S. Kouro et al., "Recent advances and industrial applications of multilevel converters," *IEEE Trans. Ind. Electron.*, vol. 57, no. 8, pp. 2553–2580, Aug. 2010.

[43] B. Li, S. Zhou, D. Xu, S. J. Finney, and B. W. Williams, "A hybrid modular multilevel converter for medium-voltage variable-speed motor drives," *IEEE Trans. Power Electron.*, vol. 32, no. 6, pp. 4619–4630, Jun. 2017.

[44] B. Li, J. Hu, S. Zhou, and D. Xu, "Hybrid back-to-back MMC system for variable speed AC machine drives," *CPSS Trans. Power Electron. Appl.*, vol. 5, no. 2, pp. 114–125, Jun. 2020.

[45] M. Basić, M. Utvić, and D. Dujic, "Hybrid modular multilevel converter design and control for variable speed pumped hydro storage plants," *IEEE Access*, vol. 9, pp. 140050–140065, 2021.

[46] S. Du, B. Wu, and N. Zargari, "A control strategy for star-channel modular multilevel converter in variable-speed motor drive application," *IEEE Trans. Ind. Electron.*, vol. 66, no. 7, pp. 5094–5101, Jul. 2019, doi: 10.1109/TIE.2018.2868309.

[47] S. Du, B. Wu, and N. Zargari, "Delta-channel modular multilevel converter for a variable-speed motor drive application," *IEEE Trans. Ind. Electron.*, vol. 65, no. 8, pp. 6131–6139, Aug. 2018, doi: 10.1109/TIE.2018.2793212.

[48] M. S. Diab, A. M. Massoud, S. Ahmed, and B. W. Williams, "A modular multilevel converter with ripple-power decoupling channels for three-phase MV adjustable-speed drives," *IEEE Trans. Power Electron.*, vol. 34, no. 5, pp. 4048–4063, May 2019, doi: 10.1109/TPEL.2018.2858003.

Nageswara Rao Karaka (Student Member, IEEE) received the B.Tech. degree in electrical engineering from the Jawaharlal Nehru Technological University, Kakinada, India, in 2014, and the M.Tech. degree in industrial electronics from the National Institute of Technology Rourkela, Odisha, India, in 2018. He is currently working toward the Ph.D. degree in electrical engineering with the Department of Electrical Engineering, Indian Institute of Technology Bombay, Mumbai, India.

His research interests include multilevel converters, power electronic systems especially for grid integration, ac variable speed drives, and wind energy conversion systems.

Ibhan Chand Rath (Student Member, IEEE) received the B.Tech. degree in electrical and electronics engineering from the International Institute of Information Technology, Bhubaneswar, India, in 2014, and the Ph.D. degree in electrical engineering from the Indian Institute of Technology (IIT), Bombay, India, in 2024.

He is currently working as System Integration & Testing Consultant with the Igrenenergi Services Private Limited, Research Park, IIT Bombay. His research interests include power electronic converters for FACTS applications, grid integration of renewable energy sources, multilevel converters, active cell balancing of battery packs, battery management systems, battery energy storage systems, and multiport electric vehicle charging station applications.

Anshuman Shukla (Senior Member, IEEE) received the M.Tech. and Ph.D. degrees in electrical engineering from the Indian Institute of Technology Kanpur, Kanpur, India, in 2003 and 2008, respectively.

From 2008 to 2011, he was a Scientist with the ABB Corporate Research Center, Västerås, Sweden. In 2008, he was a Research Associate with the Department of Electrical Engineering, University of South Carolina, Columbia, SC, USA. In 2011, he joined the Indian Institute of Technology Bombay, Mumbai, India, where he is currently a Professor with the Department of Electrical Engineering. His research interests include multilevel converters, power electronics for HVdc and FACTS applications, grid-connected renewable energy systems, solid-state transformers, hybrid and solid-state circuit breakers, motor drives, and the application of SiC power electronics.

Dr. Shukla was the recipient of the 2021 Technology Translation Award conferred by SERB, Government of India, and 2011 Young Engineer Award conferred by the Institution of Engineers, India. He is also the recipient of the MeiTy Visveswaraya Young faculty research fellowship. He is an Associate Editor for IEEE JOURNAL OF EMERGING AND SELECTED TOPICS IN POWER ELECTRONICS.